



Characterization of Hot-Extruded Mg–Gd–Y–Zn–Zr Alloy Containing a Novel Lamellar Structure and Related High Elevated-Temperature Mechanical Properties

Xu Wang^{1,2} · Yongxing Zhao^{1,2} · Yuanchun Huang^{1,2}

Received: 6 November 2022 / Accepted: 6 January 2023 / Published online: 6 February 2023
© The Author(s) under exclusive licence to The Korean Institute of Metals and Materials 2023

Abstract

Hot extrusion was introduced to the Mg–10Gd–3Y–1.5Zn–0.5Zr alloy and microstructure evolution, texture configuration and elevated-temperature mechanical properties were investigated. The results show that the LPSO phase network-distributed along grain boundaries in the as-cast and homogenized alloys is broken and elongated after extrusion, and is streamlined along the extrusion direction (ED). After extrusion, a completely recrystallized microstructure with equiaxed grains of ~10 μm is formed. The most notable feature in as-extruded alloy is numerous fine lamellar structures in DRXed grains, which were identified as basal stacking faults (SFs) with nano-spaced by TEM analysis. The <0001>//TD texture results in the hard orientation of most grains along ED. The extruded alloy exhibits excellent elevated-temperature mechanical properties (UTS/287 MPa and YS/218 MPa at 300 °C; UTS > 200 MPa at 350 °C) along ED, which is significantly higher than alloys with similar composition or even higher rare earth content. The high elevated-temperature strength is mainly related to the fiber strengthening effect of streamline-distributed LPSO, the skeleton support effect of numerous SFs with nano spacing, and the texture strengthening effect of hard grain orientation.

Keywords Magnesium alloy · Extrusion · Elevated-temperature · Mechanical properties · Stacking faults

1 Introduction

Magnesium alloys have imperative requisition prospects in the fields of automobile and aerospace due to the advantages of excellent creep resistance, light weight, high specific strength, etc. At the same time, the application of magnesium alloy has gradually transformed from auxiliary load-bearing components to heat-resistant structural parts. This postures a higher challenge of the high temperature properties for magnesium alloys [1–4]. However, the currently used AZ, AM, and ZK series of commercial magnesium alloys exhibit medium room temperature strength and cannot meet the high temperature performance requirements. Therefore,

developing a new series of magnesium alloys with both room temperature and high temperature properties is of great significance [5–7].

Many scholars have done quantities of research to enhance the mechanical strength of Mg alloys. The relevant results show that alloying with rare-earth (RE) addition has a positive impact on mechanical performance. In all rare-earth-containing magnesium alloys, the Mg–RE (Gd, Y, Nd, etc.)–Zn series has great potential for further development [1, 8–10]. The addition of Zn element can significantly increase the aging-response of the alloy by reducing the equilibrium solid solubility of RE elements [11]. In addition, Zn can also form a long-period-stacking-order (LPSO) structure with RE elements to greatly improve the properties [7]. As an example, the yield strength (YS) of Mg₉₃Zn₆Y₁ alloy prepared by hot extrusion and aging can reach 400 MPa [12]. Kawamura et al. [13] developed a LPSO-containing Mg₉₇Zn₁Y₂ alloy with ultra-high-strength through the rapid solidification powder metallurgy (RS P/M) method. Its YS at room temperature even exceeds 600 MPa, but with poor elongation. In recent

✉ Yuanchun Huang
ychuang@csu.edu.cn

¹ Light Alloy Research Institute, Central South University, Changsha 410083, China

² State Key Laboratory of High Performance Complex Manufacturing, Central South University, Changsha 410083, China

years, researchers have developed Mg–Gd–Y–Zn alloys, and obtained both of good room temperature strength and elongation. Honma et al. [14] successfully produced a Mg–1.8Gd–1.8Y–0.7Zn–0.2Zr alloy with the ultimate tensile strength (UTS) of 542 MPa, YS of 471 MPa, and the elongation of 8%. The excellent mechanical properties are due to the formation of fine precipitates during the extrusion and aging process. Recently, Ramezani et al. [15] obtained 581 MPa tensile strength and 15.9% elongation of Mg–8.1Gd–4.3Y–1.6Zn–0.4Zr alloy by extrusion and multi-directional forging. The ultra-fine grain structure formed by particle stimulated nucleation (PSN) mechanism due to high volume fraction of LPSO phase is the reason for its excellent mechanical properties.

Additionally, the RE-addition can form high-strength thermally stable precipitates, thus enhancing the elevated-temperature performance of Mg–RE–Zn alloys. Research had reported 250 °C/310 MPa and 300 °C/182 MPa of heat resistance properties of Mg–10Gd–3Y–0.5Zr alloy [16]. Meng et al. [17] reported a hot-extruded Mg–7Y–4Gd–1.5Zn–0.4Zr alloy, and the heat resistance is about 300 °C/230 MPa. Recently, Yang et al. [18] designed a Mg–8Gd–3Yb–1.2Zn–0.5Zr alloy by conventional hot-extruded, the UTS and YS at 300 °C can reach 204 MPa and 191 MPa, respectively. Obviously, these alloys have better RT and elevated-temperature performance than the traditional heat-resistant rare earth magnesium alloys WE43 and WE54 [19], but the strength still decreases significantly when the temperature is over 250 °C.

In the present study, conventional hot extrusion was introduced to the Mg–10Gd–3Y–1.5Zn–0.5Zr alloy fabricated by semi-continuous casting. Excellent elevated-temperature strength (the UTS is 287 MPa and YS is 218 MPa at 300 °C and the UTS is over 200 MPa even at 350 °C) is

obtained. It is noteworthy that except for the LPSO phase previously reported in most Mg–RE–Zn alloys, numerous special fine parallel lamellar structures are developed inside almost all DRXed grains. Our paper investigates the microstructure evolution and the strengthening mechanism of the elevated-temperature high performance extruded alloy.

2 Experimentation

The Mg–10Gd–3Y–1.5Zn–0.5Zr (wt%) cast ingot was produced by a semi-continuous casting method with atmosphere protection. High-purity metal Mg, Zn, and master alloys Mg–30Gd (wt%), Mg–30Y (wt%), and Mg–30Zr (wt%) were melted at ~ 750 °C. After removing the surface slag, the cylindrical ingot of $\Phi 260 \times 800$ mm was fabricated successfully, and its chemical composition was tested to be Mg–9.7Gd–2.5Y–1.5Zn–0.4Zr (wt%) using an inductivity coupled plasma atomic emission spectroscope (ICP-AES). According to our previous research [8], the solid-solution parameters are determined as 520 °C/16 h. Before extrusion, the ingot was turned to $\Phi 247$ mm and kept at 400 °C for 1 h, then direct extrusion was performed on the ingot at 400 °C with the extrusion speed of 0.3 mm/s and an extrusion ratio of 17.

The microstructure of the samples was tested via optical microscopy (OM, OLYMPOS-DSX500), scanning electron microscopy (SEM, Helios Nanolab 600i) equipped with an X-ray energy-dispersive spectrometry (EDS) system and an electron back-scattered diffraction (EBSD) system, X-ray diffraction (XRD), transmission electron microscopy (TEM, JEM-2100F). The samples for OM characterization were etched with a mixture of 4.2 g $C_6H_3N_3O_7$ + 10 mL CH_3COOH + 10 mL

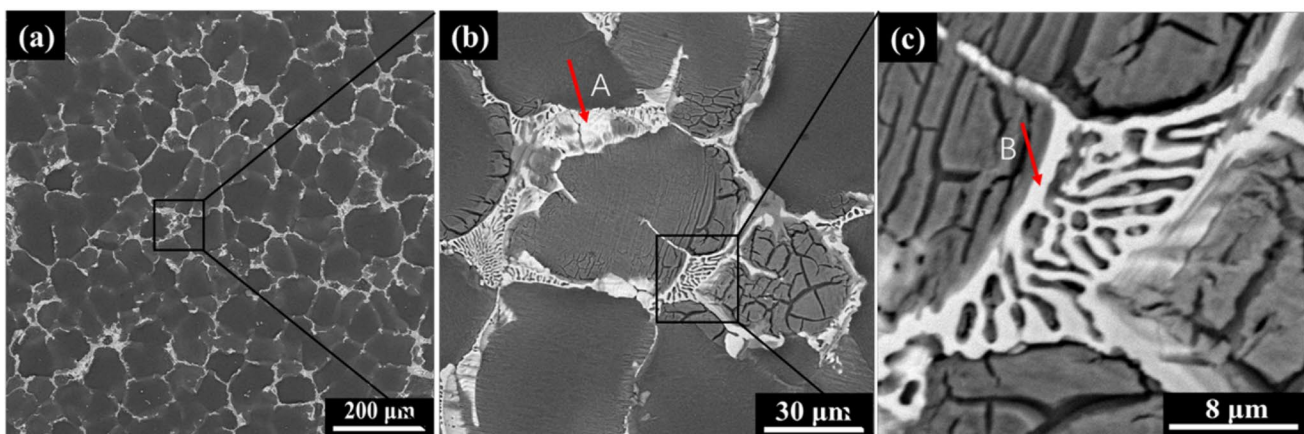


Fig. 1 SEM images of the as-cast alloy

$\text{H}_2\text{O} + 70 \text{ mL C}_2\text{H}_5\text{OH}$. Samples for EBSD observation were electropolished in a 95% $\text{C}_2\text{H}_5\text{OH} + 5\% \text{HClO}_4$ solution at about $-35 \text{ }^\circ\text{C}$ and the EBSD results were post-processed and analyzed with channel5 software. The mechanically polished sample was punched to $\Phi 3\text{mm}$ and thinned to a thickness of about $50 \mu\text{m}$, and then subjected to TEM observation after double spraying and ion thinning. The above samples were all taken from the normal direction (ND) and the extrusion direction (ED). The volume fraction of the second phase is measured by Image Pro Plus software. Cylindrical tensile specimens

of $\Phi 5 \text{ mm (diameter)} \times 25 \text{ mm (gauge length)}$ along ED were conducted to RT and elevated-temperature tensile tests with an initial strain rate of $10^{-3}/\text{s}$.

3 Results and Discussion

3.1 Microstructure of As-Cast Alloy

The SEM images of the as-cast alloy sample are shown in Fig. 1. In addition to the α -magnesium matrix, the

Fig. 2 XRD patterns of **a** as-cast, **b** solid-solution treated and **c** as-extruded alloys

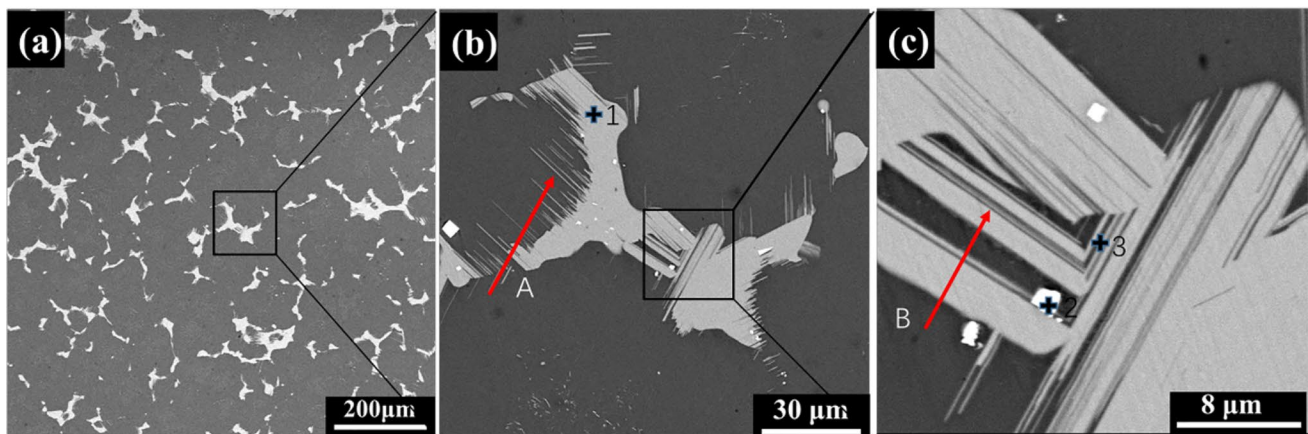
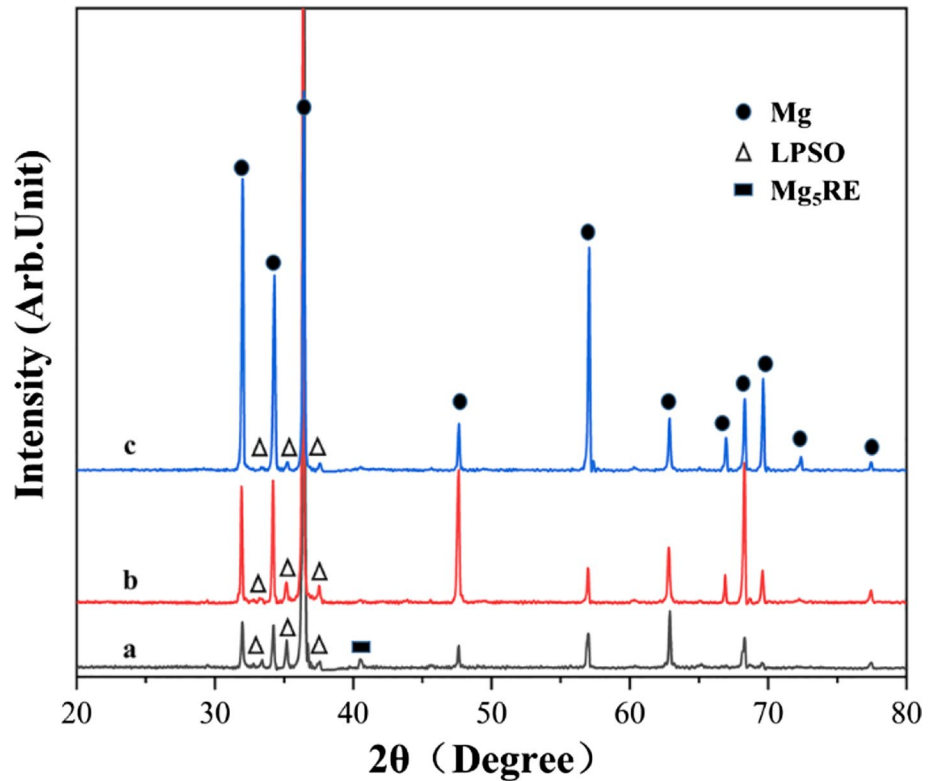


Fig. 3 SEM images of the alloy after solid-solution at $520 \text{ }^\circ\text{C}$ for 16 h

eutectic phase is continuously network-distributed at the grain boundary (Fig. 1a), and the volume fraction of the eutectic phase is about 11.82% through statistical analysis. The enlarged SEM image (Fig. 1b) shows that the eutectic phase consists of two different phases of alternating distribution: a blocky white phase (marked by arrow A) and a fishbone-shaped phase (marked by arrow B). In addition, there are many microcracks in the matrix near the eutectic phase (Fig. 1b), which is mainly related to the internal stress of the casting caused by the large size and high alloy composition of our ingot. The inconsistency of the solidification speed between the eutectic phase and magnesium matrix causes the microcracks to start near the eutectic phase and further extend to the matrix.

In order to further determine the two eutectic phases, EDS analysis was carried out on the phase components in the arrows A and B in Fig. 1. The element content of the blocky white phase (arrow A) is about Mg–3.6Gd–4.1Y–6.9Zn (at%), the atomic ratio of Mg:(Gd + Y):Zn is similar to Mg₁₂RE₁Zn₁, which is a typical LPSO phase with a 18R structure [20–22]. The element content of the fishbone-shaped phase (arrow B) is about Mg–5.9Gd–3.8Y–5.3Zn (at%). The ratio of Mg element to solid solution element (Gd, Y, Zn) in this phase is about 5.6, which is close to Mg₅(Gd, Y, Zn). Figure 2 exhibits the XRD patterns of the alloy in different states. The characteristic diffraction peaks of Mg, LPSO phase and Mg₅RE phase were detected in the as-cast alloy, which was consistent with the results of EDS. However, the peak intensity of Mg₅RE eutectic phase is not obvious, which may be due to its small volume fraction. However, the types of as-cast eutectic are of different perspectives [23, 24]. Some scholars believe that these eutectic phases are Mg₂₄RE₅ or Mg₃RE compounds, which may be related to different casting parameters [25], which needs further research.

Table 1 EDS results of phases in Fig. 3

Point	Mg (at%)	Gd (at%)	Y (at%)	Zn (at%)	Zr (at%)
1	83.6	9.6	1.8	4.9	0.0
2	36.2	23.2	39.1	1.2	0.4
3	93.9	2.0	1.5	2.6	0.0

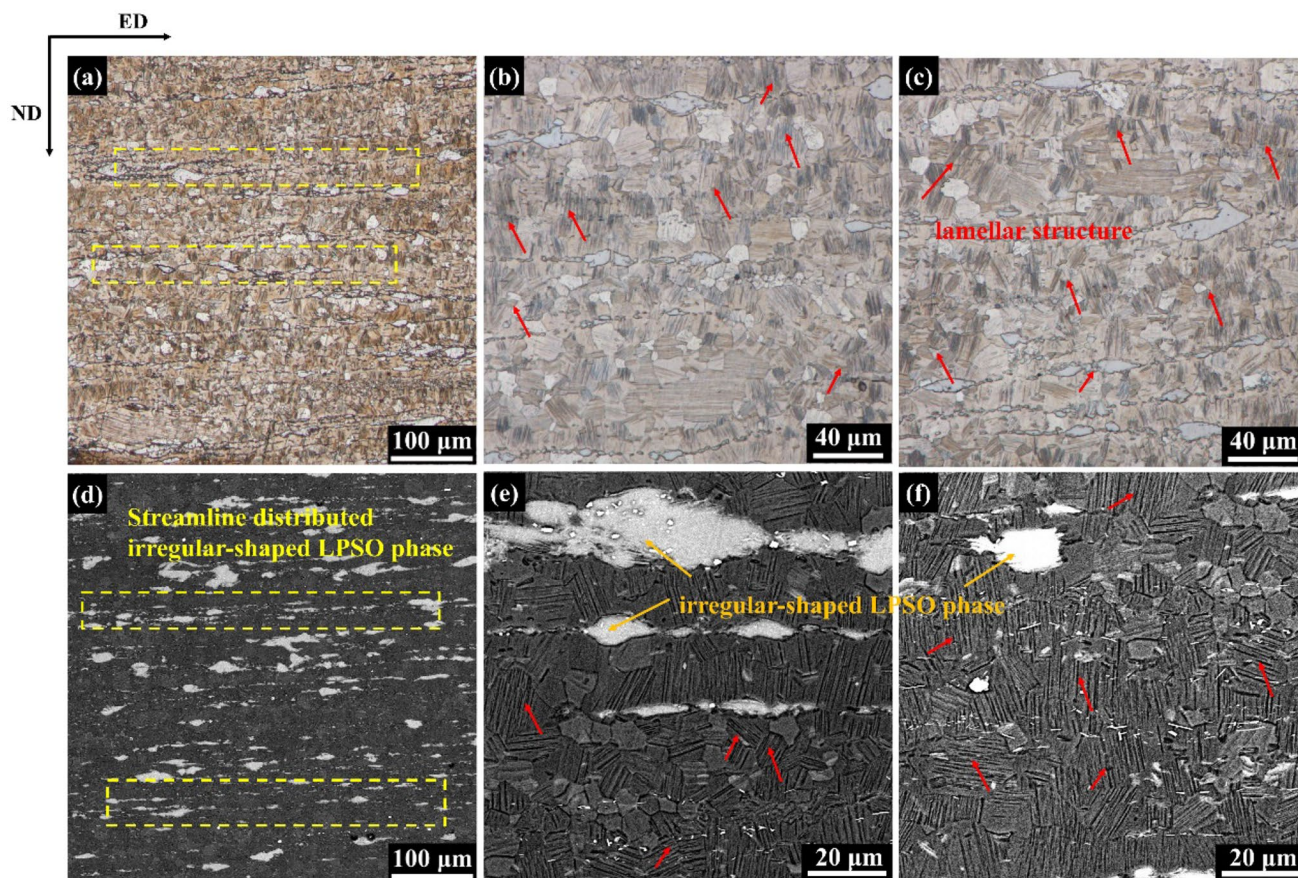


Fig. 4 OM and SEM images of the as-extruded alloy

3.2 Microstructure of Solid-Solution Alloy

According to our previous study [8], the final solution parameters were determined as 520 °C/16 h. Figure 3a, b, c show the SEM images of the microstructure of solid-solution alloy samples. Compared with the as-cast alloy, the second phase is semi-continuously network distributed after solution (Fig. 3a), and the volume fraction also decreases to 9.07%, which indicates that the coarse eutectic phase gradually dissolves into the matrix during the solution. From Fig. 3b, the second phase is mainly in a block shape at grain boundary, and extends into the α -Mg matrix in a lamellar shape (marked by arrow A), and some lamellae are coarsened and overlapped with another oriented lamella (marked by arrow B in Fig. 3c). This will enhance the bonding of the blocky LPSO phase with the matrix and increase the critical resolved shear stress (CRSS) of basal slip, thereby partly activating the non-basal slip of the magnesium matrix and improving the plasticity of the alloy [26]. EDS results of characteristic parts are shown in Table. 1. XRD pattern (Fig. 2) shows that the characteristic peak of Mg_5RE eutectic phase disappears and only LPSO phase is detected except α -Mg matrix. Studies have also

shown that in the heat-treated Mg–RE–Zn alloy, the blocky phase has a 14H-type LPSO structure, and the lamellar phase is also the 14H-LPSO phase [10, 27, 28]. Tao Chen et al. [29] studied the homogenization treatment process of Mg–1.2Zn–3.4Y–4.7Gd–0.5Zr ingot. It is believed that the formation of 14H-LPSO phase is mainly realized by $Mg_5(Gg, Y, Zn)$ and 18R-LPSO phase via phase transformation processes. This is consistent with our observations. At the same time, a small amount of bright white square phase (Point 2) is also found, which is considered as rare-earth rich phase [30]. During the solution process, the rare earth elements diffuse from the grain boundary to the grain, which provides an elemental guarantee for the formation of the square phase.

3.3 Microstructure of Alloy After Extrusion

Figure 4 exhibits the microstructure of the Mg–10Gd–3Y–1.5Zn–0.5Zr alloy after direct extrusion (400 °C). It is obvious that the second phase is broken and elongated during the extrusion process, and is streamline distributed along the extrusion direction, as shown in the yellow rectangle box in Fig. 4a, d. At the same time,

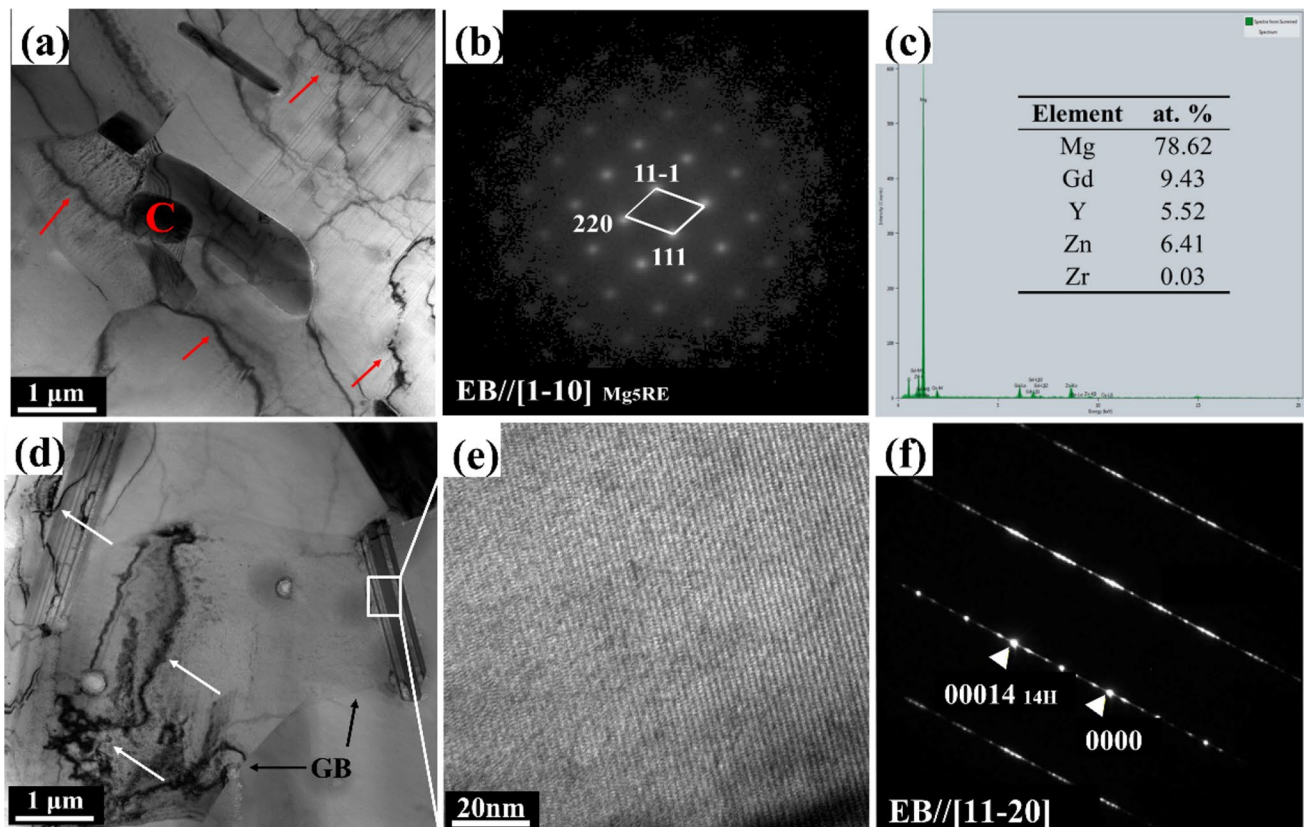


Fig. 5 TEM analysis of different phase of the as-extruded alloy: **a** and **d** BF-TEM images; **b** and **f** SEAD patterns; **c** EDS data from the phase marked C in **a**; **e** HR-TEM image of **d**

the shape of these blocky phases with variant phase sizes becomes extremely irregular (Fig. 4e), which is related to inhomogeneous deformation and metal flow in the extrusion process. According to EDS results of the irregular-shaped blocky phase in Fig. 4e, the chemical composition is Mg–10.9Gd–6.0Zn–2.3Y (at%), which is similar with the blocky LPSO phase of solid-solution treated alloy. Combined with the XRD results in Fig. 2, these blocky phases also belong to the LPSO phase, which should be transformed from the blocky LPSO phase network-distributed along the grain boundary in the homogenized alloy under the effect of extrusion. After extrusion, the matrix is almost completely composed of equiaxed recrystallized grains, and the grains are more refined with an average grain size of 11.7 μm compared to grains size of about 91 μm before extrusion. Notably, a needle-like lamellae structure was observed in most grains, with lamellae in the same grain having the same orientation, but the lamellae orientation of different grains being more random (marked by red arrows). Similar morphologies were observed in the study of extrusion speed by Liu et al. [25], and they believed that lamellae formed inside grains are stacking faults at low extrusion speed (0.1 m/min), when increases to 0.3 m/min, the fine lamellar structure is not stacking fault, but 14H structure. From Fig. 2, there is no obvious difference in phase type after extrusion compared to the solid-solution state, except for the intensity of the characteristic peak. Therefore, it is necessary to further detect the parallel lamellar structure in the extruded alloy.

Figure 5 shows the TEM analysis of different phases of the extruded sample. The first type is in regular shape and distributed at grain boundaries (Fig. 5a). From the SAED pattern in Fig. 5b and the EDS result marked as the point C phase in Fig. 5c, this second phase is determined to be Mg_5RE , which belongs to face-centered cubic (fcc) structure with a lattice constant of 2.23 nm [31]. Many dislocations (marked by red arrows) are distributed around these Mg_5RE phases, and the trajectory of dislocation slip can also be seen. During the deformation process, these phases can not only stimulate DRX nucleation through the PSN mechanism, but also inhibit dislocation slip and effectively pin grain boundaries, thus improving the strength at RT and high temperatures [32]. The second type is lamellar structures, with a width of 0.2–1 μm and a length of less than 3 μm , and most of them present gray contrast (Fig. 5d). Figure 5e is a high-resolution-TEM (HR-TEM) image of these fine lamellae. The corresponding SAED pattern divides the distance between the transmission spot and the $(0002)_{\alpha\text{-Mg}}$ into 7 equal parts, indicating that it has a 14H-LPSO structure [33]. It is inferred from the morphology and size that these lamellar structures were broken and detached during extrusion process, mainly distributed at the grain boundaries (GB). Dislocation entanglement was found near the GB and the LPSO phase (white arrows in Fig. 5d). The interaction

between LPSO phase and dislocation indeed exists. Matsuda et al. [26] studied the dislocation structure of rapidly solidified $\text{Mg}_{97}\text{Zn}_1\text{Y}_2$ alloy containing LPSO phase, and observed obvious dislocation aggregation and entanglement with LPSO phase at grain boundary, which is very beneficial to the strengthening of the alloy.

Figure 6a shows the BF-TEM analysis of the electron beam (EB) parallel to the $[11\text{--}20]$ Mg direction. The magnified high-angle annular dark-field scanning TEM (HAADF-STEM) and HR-TEM images are shown in Fig. 6c and Fig. 6d. It is obvious that dense and fine parallel lamellae are formed in the un-DRXed region, with the space between each other from 20 nm to 200 nm. The abnormally stacked atomic staggered surfaces in Fig. 6d together with the clear streaks in SAED patterns indicates these fine parallel lamellae belongs to stacking faults (SFs) and they may form during the hot extrusion process due to solute segregated [34, 35]. Furthermore, these SFs are observed to pin the dislocations effectively by numerous dislocation entanglements occupying the dark contrast band in Fig. 6a. Figure 7 displays TEM images of a typical DRXed grain with obvious grain boundary. The parallel lamellar structures with nano-space are almost distributed in the whole grain (Fig. 7a), according to HR-TEM analysis with SEAD pattern (Fig. 7b), these fine lamellar structures are also basal plane stacking faults (SFs), which are similar as the SFs in the un-DRXed regions.

Generally, our alloy exhibits a special microstructure after extrusion. Except for the LPSO phase and blocky Mg_5RE phase, the most notable feature is that the basal plane SFs with nano-spaced are formed in both of DRXed grains and un-DRXed region. Some researchers have reported the SFs in the Mg–RE–Zn alloy. The study of E. Abe et al. proved that adding Zn and Y to Mg can form long-period chemical ordered structure and stacking ordered structure [36]. Yang et al. [37] studied the deformation stacking faults caused by dislocation dissociation at an atomic scale. They believed that the segregation of Zn/Y in Mg grains can decrease the stacking fault energy and stabilize the SFs or LPSO structure, which has a strong effect on improving the high temperature strength of the alloy. Yamasaki et al. [35] proposed a time–temperature transition diagram of Mg–Zn–Gd alloy. They believed that the formation of matrix stacking faults and 14H-LPSO phase in the saturated $\alpha\text{-Mg}$ matrix during medium and high temperature aging (above 623 K) are the reason for the strengthening of Mg–Zn–Gd alloy. Stacking faults have also been found in Mg–RE–Zn alloys after compression deformation [38]. On the one hand, after solid solution treatment, the content of solute atoms in Mg grains increased, forming chemical conditions. On the other hand, deformation can promote the formation of metastable LPSO/SFs and solute atom diffusion by inducing defects such as dislocations. However, in this study, the formation of

Fig. 6 TEM analysis of the un-DRXed region: **a** bright field (BF)-TEM images; **b** SAED pattern; **c** HAADF-STEM image; **d** HR-TEM image

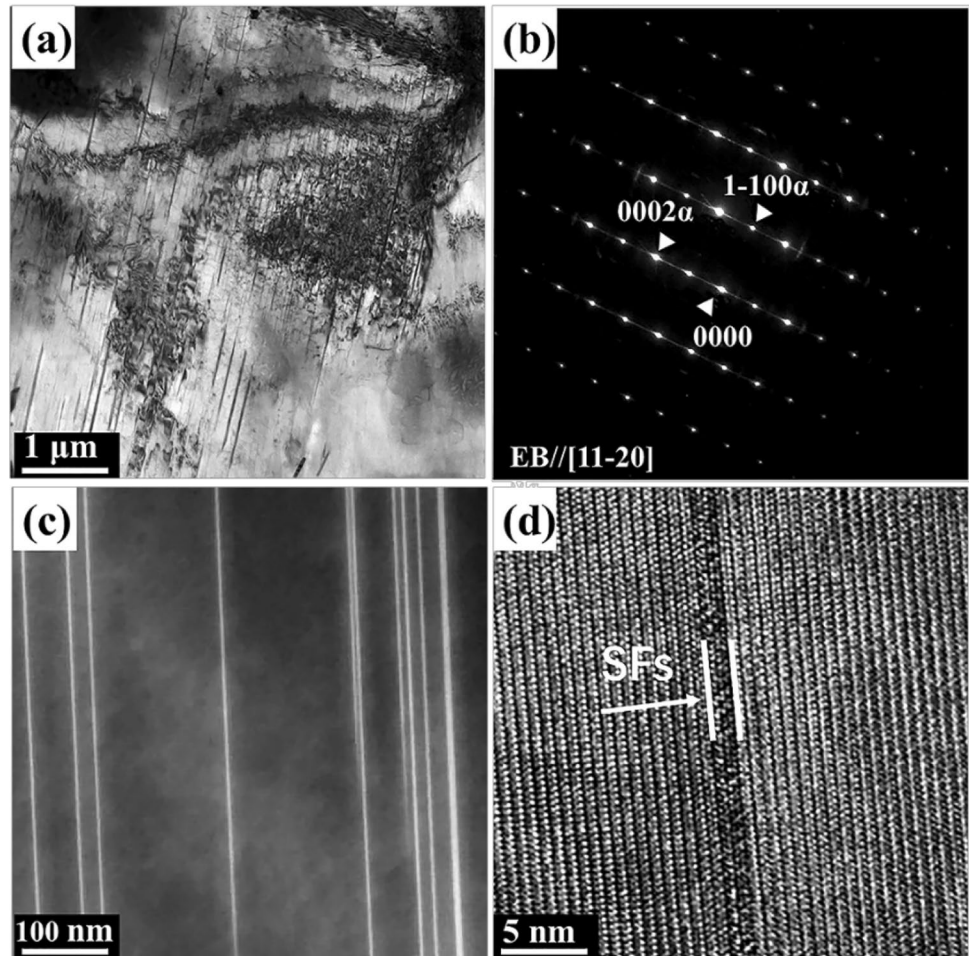
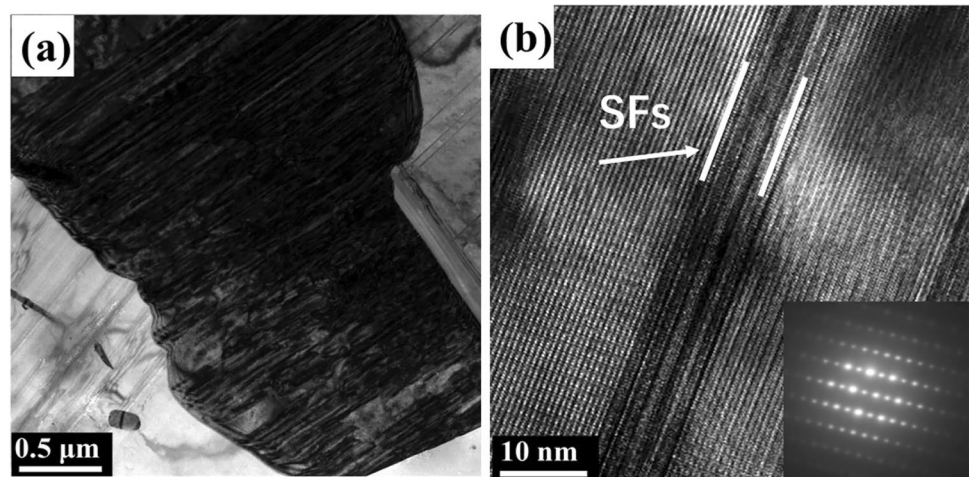


Fig. 7 TEM analysis of a typical DRXed grain: **a** BF-TEM image; **b** HR-TEM image



numerous SFs in the DRXed grains and un-DRXed regions after extrusion has hardly been reported.

In the present work, EBSD analysis was also conducted on the grain information of the extruded samples. Figure 8a displays the inverse pole figure (IPF) of the observation surface parallel to ED, no obvious large-size deformed structure

is found, and a homogeneous microstructure of equiaxed grains is obtained. From the corresponding statistics of grain size in Fig. 8b, most of the grain sizes are below 15 μm, and the average grain size is 10.03 μm. According to the statistics of grain boundary misorientation, LAGBs account for 26.8%, and the grain boundary is mainly black lines

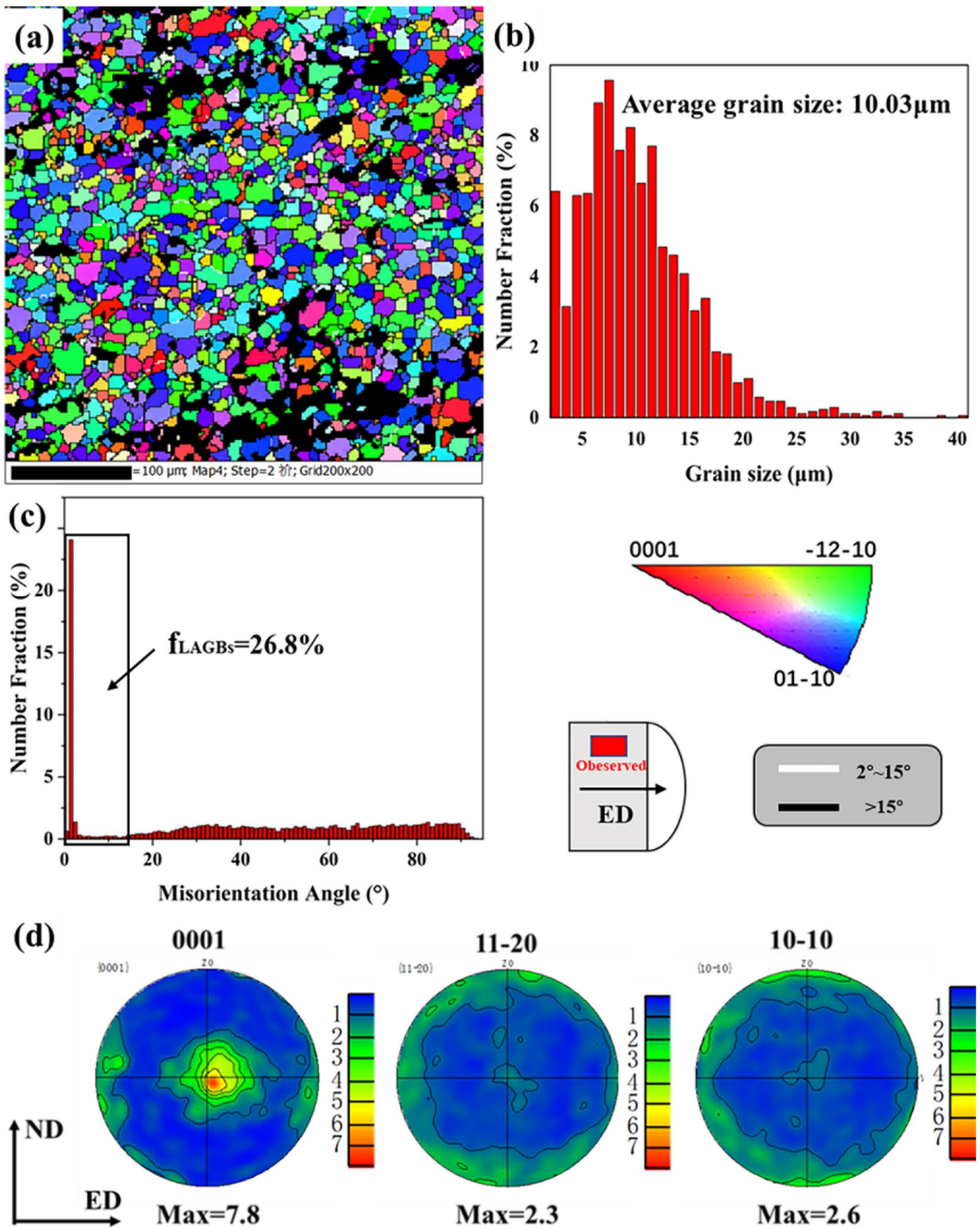


Fig. 8 EBSD analysis of the as-extruded alloy: **a** IPF of superimposed grain boundaries; **b** grain size distribution; **c** misorientation angle distribution; **d** pole figures with maximum intensity noted below. The black area in the IPF diagram represents the unresolved

phase region, and the high angle grain boundary (HAGBs) and low angle grain boundary (LAGBs) are shown with black and white lines respectively

representing HAGBs (Fig. 8a), indicating that the sample is completely recrystallized. In addition, the grain orientation is dominated by blue and green, combined with the pole figure (PF) of Fig. 8d, a c -axes//TD orientation of the majority grains with a maximum pole intensity peak of 7.8 is obtained, while a small part of the c -axes is around ED with a much weaker pole intensity. The high RE content in our alloy may be responsible for the abnormal $\langle 0001 \rangle$ //TD texture. Grain boundary segregation and low diffusion of RE atoms hinder the movement of grain boundaries and dislocations, resulting in the change of texture [39]. In addition, the activation of non-basal slip during hot deformation also hinders the movement of dislocations on the basal plane, which also leads to texture modification. The change of deformation mode will be discussed in more depth below.

It is generally believed that grains with different crystal orientations lead to different deformation modes. Slips and twins are more likely to activate during the deformation of polycrystalline Mg alloy. However, almost no twinning was observed in our extruded alloys, which may be related to the texture configuration of $\langle 0001 \rangle$ //TD and numerous lamellar structures. The orientation of $\langle 0001 \rangle$ //TD results in the direction of vertical to ED of most grains c -axis, which inhibits the formation of tensile twins during

extrusion. In addition, the presence of numerous lamellar structures in our alloys also inhibit the growth of twins. It has been reported that the densely distributed lamellar LPSO phase in the rapidly solidifying Mg–Zn–Y alloy allows the $\{10\text{--}12\}$ twin nucleus to grow only along the lamellar edges, which greatly limits the combined growth and coarsening of the twins [40]. Therefore, we study three main slip modes of (0001) $[11\text{--}20]$ basal slip, $\{1\text{--}100\}$ $[11\text{--}20]$ Prismatic slip and $\{11\text{--}22\}$ $[-1\text{--}123]$ pyramidal slip. Figure 9 shows the Schmid factor (SF) maps and distributions of the three slip modes of the as-extruded sample. Obviously, the SF distribution of the basal $\langle a \rangle$ slip is very uniform, while high SF of the prismatic $\langle a \rangle$ slip and the pyramidal $\langle c + a \rangle$ slip account for a relatively large amount, especially for the pyramidal $\langle c + a \rangle$ slip. Therefore, the average SF of basal $\langle a \rangle$ slip is the lowest, only 0.276, compared to 0.324 for prismatic $\langle a \rangle$ slip and 0.413 for pyramidal $\langle c + a \rangle$ slip. Generally speaking, the larger the SF value, the easier to activate the corresponding slip system in plastic deformation [41]. Consequently, the hard orientation of the basal plane increases the CRSS of the basal $\langle a \rangle$ slip, which makes it more difficult to activate basal $\langle a \rangle$ slip.

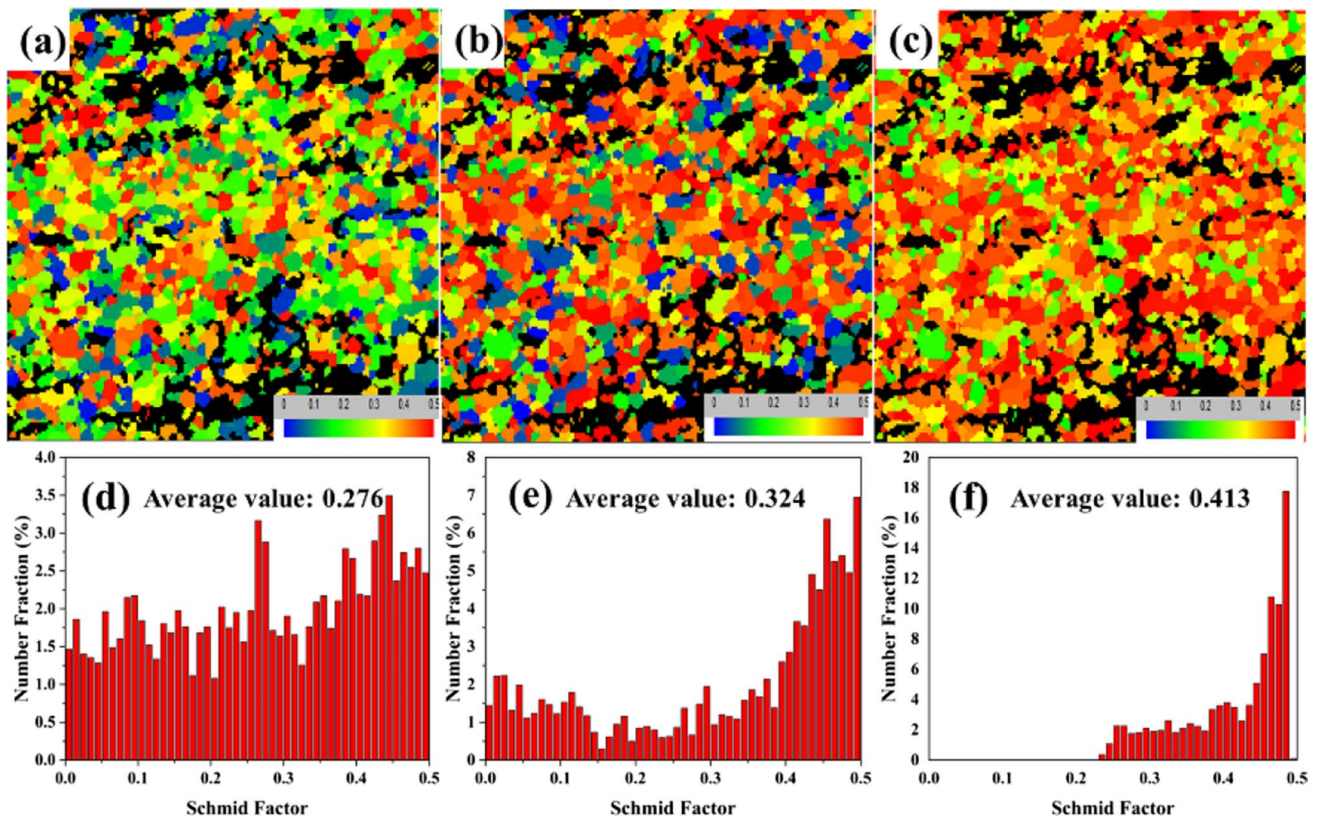


Fig. 9 Schmid factor (SF) maps concerning various slip systems and SF distributions: **a** and **d** Basal $\langle a \rangle$: $\{0001\}$ $[11\text{--}20]$, **b** and **e** Prismatic $\langle a \rangle$: $\{1\text{--}100\}$ $[11\text{--}20]$, **c** and **f** Pyramidal $\langle c + a \rangle$: $\{11\text{--}22\}$ $[-1\text{--}123]$

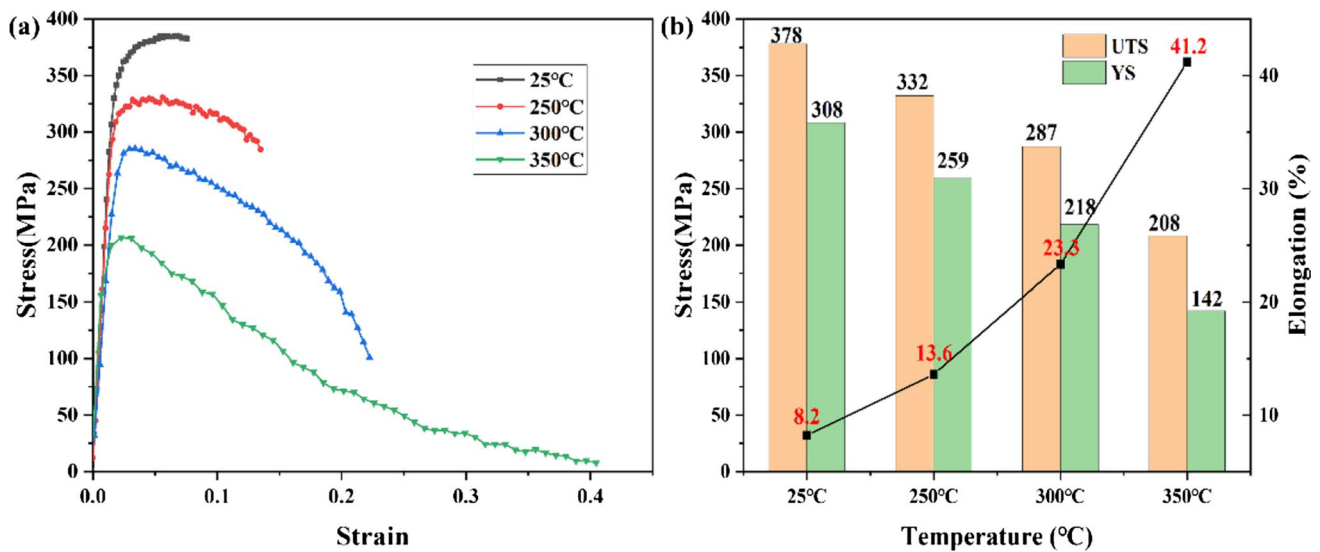


Fig. 10 Tensile properties of the as-extruded alloy at different temperatures

3.4 Mechanical Properties

The room temperature (RT) and elevated temperature properties of our extrusion alloy are illustrated in Fig. 10. Excellent elevated temperature tensile properties are obtained. At RT, while obtaining 378 MPa of the ultimate tensile strength (UTS) and 308 MPa of yield strength (YS), the elongation (E) can exceed 8%. A ~290 MPa of UTS can remain at 300 °C, and its elongation increases by 184%. When the temperature reaches 350 °C, the strength of the alloy decreases rapidly, but its UTS can still be maintained above 200 MPa. This excellent high-temperature property has rarely been reported in wrought magnesium alloys.

The SEM of the cross-sections of tensile samples at different temperatures are shown in Fig. 11. It is obvious that the fracture depth of the cross-section increases with increasing tensile temperature (Fig. 11a1–d1), 126 μm, 177 μm, 186 μm and 355 μm for RT, 250 °C, 300 °C and 350 °C, respectively, showing different fracture mechanisms. The microstructure of RT and 250 °C tensile samples are similar, with relatively flat fracture section, and a large number of lamellar structures with different orientations still exist (the red lines display the lamellar orientation), which, according to their morphology and distribution, are SFs and have high thermal stability at 250 °C. The intergranular irregular-blocky-shaped LPSO phase is still streamline distributed along the tensile direction, and fracture cracks were found at the striped LPSO near the fracture surface, which cut across the LPSO and at approximately 45° to the tensile direction (at the yellow arrow), which is consistent with the direction of the maximum critical resolved shear stress (CRSS) during tension. When the tensile temperature is 300 °C, the number of SFs in the sample decreases, and SFs tend to distribute

parallel to tensile direction, the matrix occurs flow behavior, and the flow trace are shown as the white lines. In addition, no shear cracks are found at the blocky LPSO, but numerous drag holes are more prone to appear at the interface between the blocky LPSO and the matrix, with a chain-distributed along tensile direction (yellow ellipse). As for 350 °C, SFs are almost completely parallel to the tensile direction, the flow behavior of the matrix is more obvious, and the grain boundaries are no longer visible. More chain-like drag holes occur, extend and merge, resulting in increasing holes size even more than 25 μm.

The schematic diagrams of the deformation mechanisms at different tension temperature are demonstrate in Fig. 12. At RT and 250 °C, the lower deformation temperature cannot effectively activate the non-basal slip, so the dominant deformation mechanism is still basal slip. However, numerous lamellar SFs in the matrix due to solute segregation can effectively pin dislocations by providing more dislocation pinning sites. Meanwhile, as depicted in Fig. 11a3, a4, b3, b4, the parallel lamellar SFs inside the DRXed grains can also support the grains like a skeleton and limit the rotation of the crystal lattice, while the SFs in the un-DRXed regions hinder the sliding of the grain boundary, which provides a significant strengthening effect, making the deformation of the matrix more difficult, which further increases the strain incompatibility between the matrix and the irregular blocky LPSO with high modulus. Therefore, the LPSO and matrix are more prone to shear fracture of ~45° to tension direction under the effect of CRSS, and the inhibition of non-basal slip also leads to a flatter fracture cross section, which is related to the dominated deformation mechanism by shear fracture (Fig. 12b). When tension at 300 °C, the CRSS of non-basal slip is significantly reduced, which makes it easier

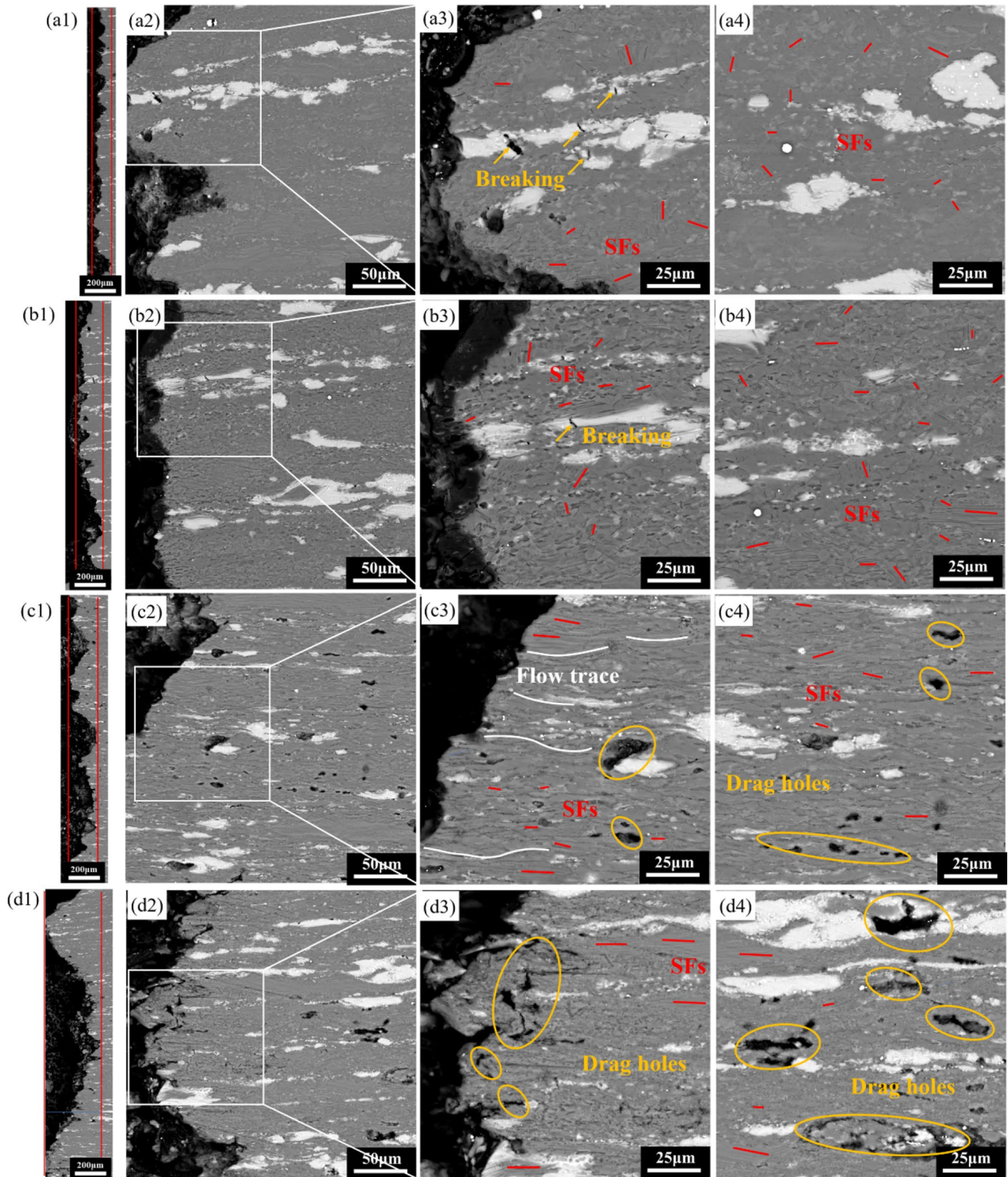


Fig. 11 Microstructure of cross-section of different temperature tensile samples: **a1–a4** RT; **b1–b4** 250 °C; **c1–c4** 300 °C; **d1–d4** 350 °C

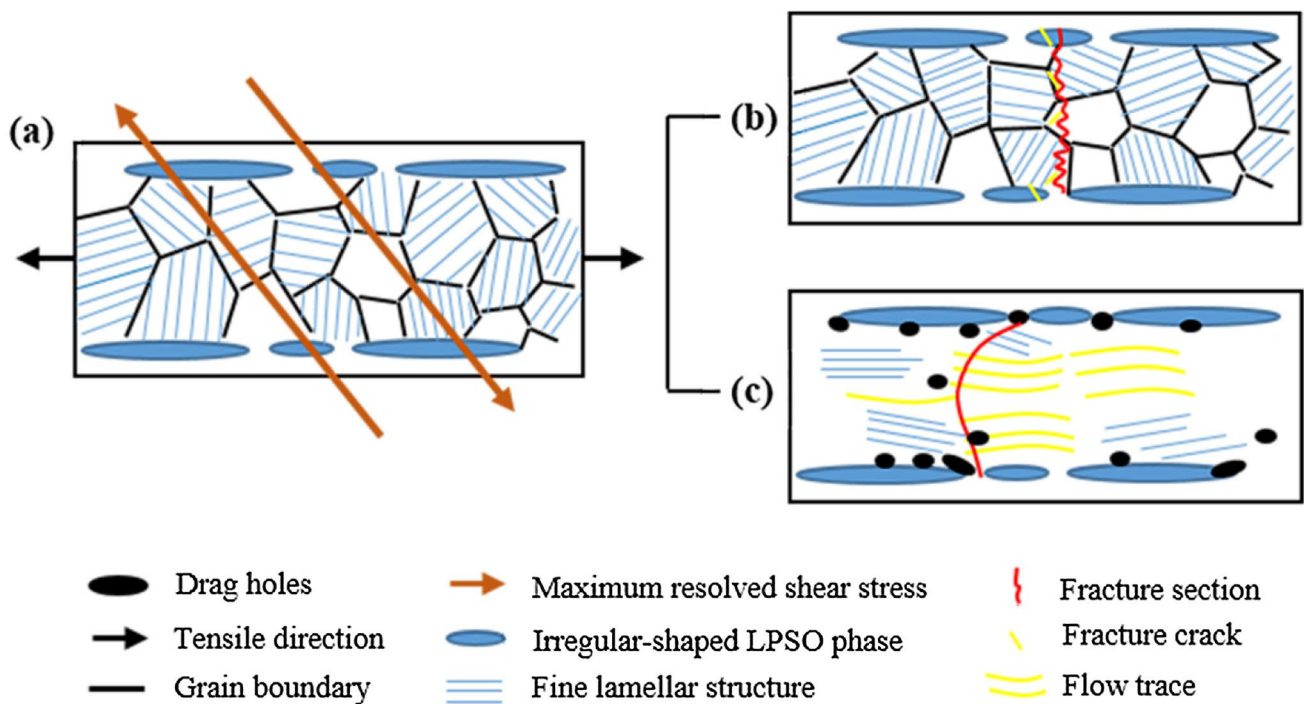


Fig. 12 Schematic diagram of the deformation mechanisms at different tension temperature: **a** as-extruded; **b** RT and 250 °C; **c** 300 °C and 350 °C

to activate [50], greatly improving the strain compatibility of the matrix, so that the flow behavior of the matrix occurs, and the grains containing SFs tend to rotate to the direction parallel to tension to resist the shearing stress. Meanwhile, the blocky LPSO phase has higher modulus, and the preferential deformation mode of (0001) <11–20> slip of

LPSO phase in 77–673 K also makes the slip more difficult than that of Mg matrix [47], thus the blocky LPSO is less prone to shear fracture, but is easy to form drag holes at the interface with the matrix. When the tensile temperature further increases to 350 °C, the activation of more non-basal slip improves the plastic deformation ability of the alloy,

Table 2 Tensile properties (UTS, YS and E) of our alloy and other typical heat-resistant extrusion Mg alloys with similar compositions

Alloys (wt%)	Temperature (°C)	UTS (MPa)	YS (MPa)	E (%)	References
Mg–5Gd–3.1Y–2.1Zn–0.5Zr	200	294	196	18.6	[42]
	300	237	182	30.1	
Mg–11Gd–4.5Y–1Nd–1.5Zn–0.5Zr	250	286	268	10.5	[43]
	300	193	172	54.4	
Mg–8Gd–2Y–1Nd–0.3Zn–0.6Zr	200	233	134	20.1	[44]
	300	188	121	44	
Mg–8Gd–3Yb–1.2Zn–0.5Zr	250	334	314	13	[18]
	300	204	191	25.5	
Mg–12Gd–3Y–0.5Zr	250	324	237	8.6	[19]
	300	225	178	17.8	
Mg–7Y–4Gd–1.5Zn–0.4Zr	250	316	282	19	[17]
	300	231	127	39	
Mg–9.7Gd–2.5Y–1.5Zn–0.4Zr	RT	378	308	8.2	
	250	332	259	13.6	This work
	300	287	218	23.3	
	350	208	142	41.2	

resulting in a more obvious flow behavior of the matrix, and the SFs are almost completely parallel to the tensile direction to resist deformation, the number of drag holes further increases, and the adjacent chain-like holes are also more likely to expand along the tensile direction, forming large-size drag holes and thus causing final fracture, at which time the alloy is dominated by plastic fracture caused by the expansion and fusion of micro holes, and the fracture section forms a deeper necking (Fig. 12c).

The tensile properties (UTS, YS and E) of our alloy and other typical heat-resistant magnesium alloys reported are listed in Table. 2 to compare the high-temperature strength more intuitively. It is found that the strength of our alloy is significantly higher than alloys with similar composition or even higher rare earth content [17–19, 42–44]. Furthermore, the YS at 300 °C is almost twice that of commercial high temperature WE43 alloy (less than 150 MPa) [45]. This is related to the different strengthening effects caused by the microstructure of our alloy. Firstly, the special texture of the alloy shows a relatively low basal slip Schmid factor (Fig. 9c), the hard orientation can strongly restrain the basal slip, which requires more external force to coordinate the plastic deformation [49], leading to a higher strength in ED direction. Meanwhile, the irregular-shaped LPSO phase is streamlined along ED after extrusion, thus the fiber reinforcement will be stimulated by LPSO phase due to the maximum resolved shear stress just cuts through the streamline-distributed LPSO phase when tensile parallel to ED [46], as depicted in Fig. 12a. It is also reported that LPSO has better thermal stability than pure magnesium [48], and can effectively limit the movement of dislocations and grain boundaries even at high temperature, thus greatly improving the high-temperature performance. Meanwhile, as depicted in Fig. 12, the parallel layered SFs inside the DRXed grains can also support the grains like a skeleton and limit the rotation of the crystal lattice, while the SFs in the un-DRXed regions hinder the sliding of the grain boundary, which provides a significant strengthening effect. In addition, parallel lamellae tend to align in the tensile direction (Fig. 12b, c) during high-temperature tensile, which also results in extra fiber strengthening. Also, the SFs have high thermal stability as the basal LPSO phase [35], which ensures a good strengthening effect on the high temperature performance of the alloy even at 350 °C. As a contrast, most of the previously reported heat-resistant magnesium alloys are Mg–RE–Zn alloys without SFs [18, 43], in which the strengthening mechanism is the basal blocky LPSO phase and the nano- β phase precipitated on prismatic surface. Compared with irregular-LPSO phase, it is believed that numerous SFs with nano-spaced contribute more to the high temperature strength of the alloy by more effective pinning of dislocations and stabilizing grain structure [51]. Therefore, the unique structure formed in our alloy

(numerous basal SFs) is the main reason for obtaining excellent elevated-temperature tensile strength.

4 Conclusions

A conventional hot extrusion was introduced to the Mg–10Gd–3Y–1.5Zn–0.5Zr alloy fabricated by semi-continuous casting. Excellent elevated-temperature strength was obtained and the microstructure evolution and the strengthening mechanism were discussed. The main conclusions following can be reached:

- (1) The eutectic phase with network-distributed at grain boundary of as-cast alloy transforms into blocky LPSO phases through solution treatment. After extrusion, no obvious large-size deformed structure is found, and a homogeneous microstructure of equiaxed grains (10 μm) is obtained with the irregular-shaped blocky LPSO streamlined along ED. Furthermore, the most notable feature is the formation of the numerous fine lamellar structures in DRXed grains, which were identified as basal plane SFs with nano-spaced by TEM analysis.
- (2) A special texture with c-axes//TD of the majority grains and c-axes around ED of a small part of grains is detected. Meanwhile, the higher SF of non-basal slip makes it easier to activate than the basal slip when stretching along ED.
- (3) Excellent elevated-temperature strength of as-extruded alloy (UTS/287 MPa and YS/218 MPa at 300 °C; UTS > 200 MPa at 350 °C) is obtained, which is mainly related to the fiber strengthening effect of streamlined-distribution irregular-shaped LPSO and the skeleton support effect of numerous SFs with nano spacing in the DRXed grains. The hard orientation along ED by the $\langle 0001 \rangle$ //TD texture also has a strengthening effect.

Acknowledgements The authors are grateful for the financial supported by The National Natural Science Foundation of China (U1837207).

Authors Contribution XW was involved in conceptualization, investigation, methodology, results analysis, writing original draft. YH contributed to funding acquisition, review and editing, project administration. YZ was involved in investigation, validation and methodology.

Funding National Natural Science Foundation of China, U1837207, Yuanchun Huang.

Data Availability The data that support the findings of this study are available on request from the corresponding author. The data are not publicly available due to privacy or ethical restrictions.

Declarations

Conflict of interest On behalf of all authors, the corresponding author states that there is no conflict of interest.

References

- B.Q. Shi, L.Y. Zhao, X.L. Shang, B.H. Nie, D.C. Chen, C.Q. Li, Y.Q. Cheng, Reduction effect of final-pass heavy reduction rolling on the texture development, tensile property and stretch formability of ZWK100 alloy plates. *J. Mater. Sci. Technol.* **111**, 211–223 (2022)
- H.T. Jeong, W.J. Kim, The hot compressive deformation behavior of cast Mg–Gd–Y–Zn–Zr alloys with and without LPSO phase in their initial microstructures. *J. Magnes. Alloys* **10**, 2901–2917 (2022)
- H. Du, F. Li, P. Huo, Y. Wang, Microstructure evolution and ductility improvement mechanisms of magnesium alloy in interactive alternating forward extrusion. *Trans. Nonferrous Met. Soc. China* **32**(8), 2557–2568 (2022)
- X. Ren, Y. Huang, X. Zhang, H. Li, Y. Zhao, Influence of shear deformation during asymmetric rolling on the microstructure, texture, and mechanical properties of the AZ31B magnesium alloy sheet. *Mater. Sci. Eng. A* **800**, 140306 (2021)
- B.Q. Shi, L.Y. Zhao, D.C. Chen, C.Q. Li, Y. Dong, D. Wu, R.S. Chen, W. Ke, Characterization of a novel 14H-LPSO structure and related elevated-temperature mechanical behaviors in an extruded Mg–Y–Zn–Cu alloy. *Mater. Sci. Eng. A* **772**, 138786 (2020)
- A. Lindemann, J. Schmidt, M. Todte, T. Zeuner, Thermal analytical investigations of the magnesium alloys AM 60 and AZ 91 including the melting range. *Thermochim. Acta* **382**(1), 269–275 (2002)
- G. Li, J. Zhang, R. Wu, Y. Feng, S. Liu, X. Wang, Y. Jiao, Q. Yang, J. Meng, Development of high mechanical properties and moderate thermal conductivity cast Mg alloy with multiple RE via heat treatment. *J. Mater. Sci. Technol.* **34**(7), 1076–1084 (2018)
- M. Li, Y. Huang, Y. Liu, X. Wang, Z. Wang, Effects of heat treatment before extrusion on dynamic recrystallization behavior, texture and mechanical properties of as-extruded Mg–Gd–Y–Zn–Zr alloy. *Mater. Sci. Eng. A* **832**, 142479 (2022)
- X. Wang, Y. Wang, C. Ni, Y. Fang, X. Yu, P. Zhang, Effect of Gd content on microstructure and dynamic mechanical properties of solution-treated Mg–xGd–3Y–0.5Zr alloy. *Trans. Nonferrous Met. Soc. China* **32**(7), 2177–2189 (2022)
- C. Xu, S.W. Xu, M.Y. Zheng, K. Wu, E.D. Wang, S. Kamado, G.J. Wang, X.Y. Lv, Microstructures and mechanical properties of high-strength Mg–Gd–Y–Zn–Zr alloy sheets processed by severe hot rolling. *J. Alloy. Compd.* **524**, 46–52 (2012)
- J.F. Nie, X. Gao, S.M. Zhu, Enhanced age hardening response and creep resistance of Mg–Gd alloys containing Zn. *Scripta Mater.* **53**(9), 1049–1053 (2005)
- A. Singh, Y. Osawa, H. Somekawa, T. Mukai, Ultra-fine grain size and isotropic very high strength by direct extrusion of chill-cast Mg–Zn–Y alloys containing quasicrystal phase. *Scripta Mater.* **64**(7), 661–664 (2011)
- Y. Kawamura, K. Hayashi, A. Inoue, T. Masumoto, Rapidly solidified powder metallurgy Mg(97)Zn(1)Y(2)Alloys with excellent tensile yield strength above 600 MPa. *Mater. Trans.* **42**(7), 1172–1176 (2001)
- T. Homma, N. Kunito, S. Kamado, Fabrication of extraordinary high-strength magnesium alloy by hot extrusion. *Scripta Mater.* **61**(6), 644–647 (2009)
- S.M. Ramezani, A. Zarei-Hanzaki, H.R. Abedi, A. Salandari-Rabori, R. Minarik, Achievement of fine-grained bimodal microstructures and superior mechanical properties in a multi-axially forged GWZ magnesium alloy containing LPSO structures. *J. Alloy. Compd.* **793**, 134–145 (2019)
- Q.M. Peng, Y.M. Wu, D.Q. Fang, J. Meng, L.M. Wang, Microstructures and properties of Mg–7Gd alloy containing Y. *J. Alloy. Compd.* **430**(1), 252–256 (2007)
- K. Liu, L.L. Rokhlin, F.M. Elkin, D. Tang, J. Meng, Effect of ageing treatment on the microstructures and mechanical properties of the extruded Mg–7Y–4Gd–1.5Zn–0.4Zr alloy. *Mater. Sci. Eng. A* **527**(3), 828–834 (2010)
- B. Li, K. Guan, Q. Yang, X. Niu, D. Zhang, S. Lv, F. Meng, Y. Huang, N. Hort, J. Meng, Microstructures and mechanical properties of a hot-extruded Mg–8Gd–3Yb–1.2Zn–0.5Zr (wt%) alloy. *J. Alloy. Compd.* **776**, 666–678 (2019)
- H.R. Jafari Nodooshan, G. Wu, W. Liu, G. Wei, Y. Li, S. Zhang, Effect of Gd content on high temperature mechanical properties of Mg–Gd–Y–Zr alloy. *Mater. Sci. Eng. A* **651**, 840–847 (2016)
- H. Liu, F. Xue, J. Bai, A. Ma, J. Jiang, Formation Behavior of 14H long period stacking ordered structure in Mg–Y–Zn cast alloys with different α -Mg fractions. *J. Mater. Sci. Technol.* **32**(12), 1267–1273 (2016)
- Y.M. Zhu, A.J. Morton, J.F. Nie, Growth and transformation mechanisms of 18R and 14H in Mg–Y–Zn alloys. *Acta Mater.* **60**(19), 6562–6572 (2012)
- Y.M. Zhu, A.J. Morton, J.F. Nie, The 18R and 14H long-period stacking ordered structures in Mg–Y–Zn alloys. *Acta Mater.* **58**(8), 2936–2947 (2010)
- C. Xu, M.Y. Zheng, Y.Q. Chi, X.J. Chen, K. Wu, E.D. Wang, G.H. Fan, P. Yang, G.J. Wang, X.Y. Lv, S.W. Xu, S. Kamado, Microstructure and mechanical properties of the Mg–Gd–Y–Zn–Zr alloy fabricated by semi-continuous casting. *Mater. Sci. Eng. A* **549**, 128–135 (2012)
- Q. Yang, B.L. Xiao, D. Wang, M.Y. Zheng, K. Wu, Z.Y. Ma, Formation of long-period stacking ordered phase only within grains in Mg–Gd–Y–Zn–Zr casting by friction stir processing. *J. Alloy. Compd.* **581**, 585–589 (2013)
- X. Liu, Z.Q. Zhang, W.Y. Hu, Q.C. Le, L. Bao, J.Z. Cui, Effects of extrusion speed on the microstructure and mechanical properties of Mg–9Gd–3Y–15Zn–08Zr alloy. *J. Mater. Sci. Technol.* **32**(4), 313–319 (2016)
- M. Matsuda, S. Ando, M. Nishida, Dislocation structure in rapidly solidified Mg97Zn1Y2 alloy with long period stacking order phase. *Mater. Trans.* **46**(2), 361–364 (2005)
- D.J. Li, X.Q. Zeng, J. Dong, C.Q. Zhai, W.J. Ding, Microstructure evolution of Mg–10Gd–3Y–1.2Zn–0.4Zr alloy during heat-treatment at 773 K. *J. Alloy. Compd.* **468**(1–2), 164–169 (2009)
- L. Liu, X. Zhou, S. Yu, J. Zhang, X. Lu, X. Shu, Z. Su, Effects of heat treatment on mechanical properties of an extruded Mg–4.3Gd–3.2Y–1.2Zn–0.5Zr alloy and establishment of its Hall-Petch relation. *J. Magnes. Alloys* **10**(2), 501–512 (2022)
- T. Chen, Z.Y. Chen, J.B. Shao, R.K. Wang, L.H. Mao, C.M. Liu, Evolution of LPSO phases in a Mg–Zn–Y–Gd–Zr alloy during semi-continuous casting, homogenization and hot extrusion. *Mater. Des.* **152**, 1–9 (2018)
- J. Wang, J. Meng, D.P. Zhang, D.X. Tang, Effect of Y for enhanced age hardening response and mechanical properties of Mg–Gd–Y–Zr alloys. *Mater. Sci. Eng. A* **456**(1–2), 78–84 (2007)
- N.Y. Liu, Z.Y. Zhang, L.M. Peng, W.J. Ding, Microstructure evolution and mechanical properties of Mg–Gd–Sm–Zr alloys. *Mater. Sci. Eng. A* **627**, 223–229 (2015)
- B. Li, B.G. Teng, E.D. Wang, Effects of accumulative rolling reduction on the microstructure characteristic and mechanical

- properties of Mg-Gd-Y-Zn-Zr sheets processed by hot rolling. *Mater. Sci. Eng. A* **765**, 138317 (2019)
33. M. Yamasaki, T. Anan, S. Yoshimoto, Y. Kawamura, Mechanical properties of warm-extruded Mg-Zn-Gd alloy with coherent 14H long periodic stacking bordered structure precipitate. *Scripta Mater.* **53**(7), 799–803 (2005)
 34. Y. Jono, M. Yamasaki, Y. Kawamura, Effect of LPSO phase-stimulated texture evolution on creep resistance of extruded Mg-Zn-Gd alloys. *Mater. Trans.* **54**(5), 703–712 (2013)
 35. M. Yamasaki, M. Sasaki, M. Nishijima, K. Hiraga, Y. Kawamura, Formation of 14H long period stacking ordered structure and profuse stacking faults in Mg-Zn-Gd alloys during isothermal aging at high temperature. *Acta Mater.* **55**(20), 6798–6805 (2007)
 36. E. Abe, Y. Kawamura, K. Hayashi, A. Inoue, Long-period ordered structure in a high-strength nanocrystalline Mg-1 at% Zn-2 at% Y alloy studied by atomic-resolution Z-contrast STEM. *Acta Mater.* **50**(15), 3845–3857 (2002)
 37. Z.Q. Yang, M.F. Chisholm, G. Duscher, X.L. Ma, S.J. Pennycook, Direct observation of dislocation dissociation and Suzuki segregation in a Mg-Zn-Y alloy by aberration-corrected scanning transmission electron microscopy. *Acta Mater.* **61**(1), 350–359 (2013)
 38. C. Xu, J.P. Pan, T. Nakata, X.G. Qiao, Y.Q. Chi, M.Y. Zheng, S. Kamado, Hot compression deformation behavior of Mg-9Gd-2.9Y-1.9Zn-0.4Zr-0.2Ca (wt%) alloy. *Mater. Charact.* **124**, 40–49 (2017)
 39. S.K. Das, Y. Kang, T. Ha, I. Jung, Thermodynamic modeling and diffusion kinetic experiments of binary Mg-Gd and Mg-Y systems. *Acta Mater.* **71**, 164–175 (2014)
 40. M. Matsuda, S. Ii, Y. Kawamura, Y. Ikuhara, M. Nishida, Interaction between long period stacking order phase and deformation twin in rapidly solidified Mg97Zn1Y2 alloy. *Mater. Sci. Eng. A* **386**(1), 447–452 (2004)
 41. K. Wang, J. Wang, X. Peng, S. Gao, H. Hu, L. Zeng, F. Pan, Microstructure and mechanical properties of Mg-Gd-Y-Zn-Mn alloy sheets processed by large-strain high-efficiency rolling. *Mater. Sci. Eng. A* **748**, 100–107 (2019)
 42. X. Yang, X. Zhou, S. Yu, J. Zhang, X. Lu, X. Chen, L. Lu, W. Huang, Y. Liu, Tensile behavior at various temperatures of the Mg-Gd-Y-Zn-Zr alloys with different initial morphologies of LPSO phases prior to extrusion. *Mater. Sci. Eng. A* **851**, 143634 (2022)
 43. Z.J. Yu, Y. Huang, X. Qiu, Q. Yang, W. Sun, Z. Tian, D.P. Zhang, J. Meng, Fabrication of magnesium alloy with high strength and heat-resistance by hot extrusion and ageing. *Mater. Sci. Eng. A* **578**, 346–353 (2013)
 44. X. Hou, Z. Cao, L. Wang, S. Xu, S. Kamado, L. Wang, Microstructure and mechanical properties of extruded Mg-8Gd-2Y-1Nd-0.3Zn-0.6Zr alloy. *Mater. Sci. Eng. A* **528**(25), 7805–7810 (2011)
 45. L.Y. Chen, J.Q. Xu, H. Choi, M. Pozuelo, X.L. Ma, S. Bhowmick, J.M. Yang, S. Mathaudhu, X.C. Li, Processing and properties of magnesium containing a dense uniform dispersion of nanoparticles. *Nature* **528**(7583), 539 (2015)
 46. T. Chen, Z. Chen, J. Shao, R. Wang, L. Mao, C. Liu, The role of long-period stacking ordered phases in the deformation behavior of a strong textured Mg-Zn-Gd-Y-Zr alloy sheet processed by hot extrusion. *Mater. Sci. Eng. A* **750**, 31–39 (2019)
 47. K. Hagihara, A. Kinoshita, Y. Sugino, M. Yamasaki, Y. Kawamura, H.Y. Yasuda, Y. Umakoshi, Effect of long-period stacking ordered phase on mechanical properties of Mg97Zn1Y2 extruded alloy. *Acta Mater.* **58**(19), 6282–6293 (2010)
 48. C. Xu, M.Y. Zheng, S.W. Xu, K. Wu, E.D. Wang, G.H. Fan, S. Kamado, X.D. Liu, G.J. Wang, X.Y. Lv, Microstructure and mechanical properties of Mg-Gd-Y-Zn-Zr alloy sheets processed by combined processes of extrusion, hot rolling and ageing. *Mater. Sci. Eng. A* **559**, 844–851 (2013)
 49. K. Oh-Ishi, C.L. Mendis, T. Homma, S. Kamado, T. Ohkubo, K. Hono, Bimodally grained microstructure development during hot extrusion of Mg-2.4 Zn-0.1 Ag-0.1 Ca-0.16 Zr (at.%) alloys. *Acta Mater.* **57**(18), 5593–5604 (2009)
 50. Q. Yang, B.L. Xiao, Q. Zhang, M.Y. Zheng, Z.Y. Ma, Exceptional high-strain-rate superplasticity in Mg-Gd-Y-Zn-Zr alloy with long-period stacking ordered phase. *Scripta Mater.* **69**(11), 801–804 (2013)
 51. Z. Yu, C. Xu, J. Meng, X. Zhang, S. Kamado, Effects of pre-annealing on microstructure and mechanical properties of as-extruded Mg-Gd-Y-Zn-Zr alloy. *J. Alloy. Compd.* **729**, 627–637 (2017)

Publisher's Note Springer Nature remains neutral with regard to jurisdictional claims in published maps and institutional affiliations.

Springer Nature or its licensor (e.g. a society or other partner) holds exclusive rights to this article under a publishing agreement with the author(s) or other rightsholder(s); author self-archiving of the accepted manuscript version of this article is solely governed by the terms of such publishing agreement and applicable law.